Electronic Origin of Oxygen Transport Behavior in La-Based Perovskites: A Density Functional Theory Study

Ya-Shan Zheng,[†] Min Zhang,[†] Qian Li,[†] Yi-An Zhu,[†,*] Zhi-Jun Sui,[†] De Chen,[‡] Xing-Gui Zhou[†]

[†]UNILAB, State Key Laboratory of Chemical Engineering, Shanghai Key Laboratory of Multiphase Materials Chemical Engineering, East China University of Science and Technology, Shanghai 200237, China

[‡]Department of Chemical Engineering, Norwegian University of Science and Technology, N-7491 Trondheim, Norway

ABSTRACT: Understanding the oxygen transport behavior in perovskites is of central importance for tailoring their physical and chemical properties to various practical applications. In this contribution, periodic DFT+U calculations have been performed to unravel the electronic origin of the oxygen mobility difference in La-based perovskites involving 3*d*-block transition metals from Sc through Cu. Calculated results indicate that the perovskites generally exhibit an increased reducibility on going from $LaScO_3$ to $LaCuO_3$, and the exceptionally high oxygen vacancy formation energy in $LaFeO_3$ is due to the significant lowering of the electron exchange stabilization upon reduction. The oxygen migration barrier in the first four perovskites varies from 1.2 eV to 2.1 eV while that for the later five materials is much lower and lies between 0.4 and 0.9 eV. Electronic structure analysis indicates this abrupt change in the migration barrier can be attributed to the different degrees of charge redistribution on the central transition-metal ion during the migration process. Linear scaling relations are established to show that the oxygen bulk diffusion coefficient is governed essentially by the oxygen concentration rather than by the migration barrier. The actual partial charge on the transition metal or oxygen ion explains the electronic origin of the different oxygen transport properties of La-based perovskites, and the observed trend can be described by using the oxygen vacancy formation energy as a good descriptor.

1. Introduction

Perovskite-type oxides (ABO_3) constitute probably the best known and most widely studied mixed oxides in chemistry[1], where the A-site cation can be a rare earth, alkaline earth, or alkali cation and the B-site cation usually comes from the transition-metal elements in periods 4, 5, and 6 in the periodic table. Among the major advantages of perovskites are the stability and flexibility of their well-defined crystal structures. The ability to accommodate various substituents and dopants allows us to manipulate the materials by changing the elemental composition and oxidation state, which in turn makes it possible to tailor the physicochemical properties of the mixed oxides to their potential applications as cathode materials in solid oxide fuel cells (SOFCs)[2], catalysts and oxygen carriers in heterogeneous catalysis[3], oxygen separation membranes[4], and solid-state gas sensors[1].

In most of these applications, a shared process is the oxygen transport in bulk perovskites, and the mobility of the oxygen ions often determines how the mixed oxides function and react. For instance, SOFCs typically operate at a high temperature between 800 and 1000 °C, which is due to the fact that the lack of ionic conductivity of the traditional cathode materials limits the oxygen reduction reaction (ORR) only to the active sites very close to the triple point boundary between oxygen, the electrode, and the electrolyte[5-8]. High operating temperature, however, may lead to mechanical incompatibility of the components in the electrical device that have different thermal expansion coefficients. Hence, a very active area of current research is to develop intermediate-temperature SOFCs working at 500 - 800 °C. In this temperature range, mixed ionic-electronic conductivity (MIEC)[8] is required for the cathode material to achieve a reasonable electrochemical performance. The facile oxygen bulk transport may result in an increased active surface area, thus improving the ORR kinetics. By a similar redox mechanism, perovskite-based MIEC membranes have recently been used to separate oxygen from air at high temperatures, and the integration of oxygen production with catalytic reaction is found to be a promising strategy for upgrading methane and alkenes by selective oxidation[9]. In the catalytic dense membrane reactor, the oxygen transport in the thin membrane occurs via the hopping of the oxygen ions to their neighboring vacant sites, whereas the bulk diffusion of any other species is not permitted[10-11]. Clearly, the oxygen permeation flux and selectivity of the composite membranes depend strongly on the oxygen transport properties of the constituent perovskites. As another example, La-based perovskites are promising catalysts for the partial oxidation of methane by the chemical looping process[12]. Through a transient kinetic study, the particle size of $LaFeO_3$, and hence the

oxygen transport kinetics in the catalyst particle, was found to have a major impact on the surface oxygen content and the catalyst selectivity. Fe sites that have a high coordination number with surface oxygen are active for the total combustion of methane, whereas those surrounded by a sufficiently large number of oxygen vacancies are responsible for carbon deposition and catalyst deactivation. Only in the situation that Fe sites are moderately coordinated to surface oxygen can the partial oxidation reaction take place.

It has long been recognized that the oxygen diffusion in perovskites follows a vacancy-mediated mechanism, in large part because the size difference between transition metal and oxygen ions is not sufficiently significant to allow the occupation of interstitial sites[13]. According to the Nernst-Einstein equation, the oxygen diffusion coefficient in perovskites can be expressed in terms of the vacancy concentration and vacancy diffusion coefficient, which are governed by the strength of the metal-oxygen bonds involved and the minimum energy required to surmount the migration barrier, respectively. Thus, two related and experimentally measurable quantities are commonly used to explain and predict the oxygen transport behavior in the mixed oxides: oxygen vacancy formation energy and vacancy migration barrier. The lower the two energetic properties, the more readily can oxygen ions migrate. However, although this connection is particularly useful for the rational fabrication of ceramic materials, understanding of the physical origin of different oxygen transport properties is still very limited.

Theoretically, the density functional theory plus U (DFT+U) method has been used by Pavone et al. to explore the formation of oxygen vacancies in $LaMO_3$ (M = Cr, Mn, Fe, and Co)[14], who claimed that both the experimentally measured M-O diatomic bond strength and the negative of the M^{2+} ionization potential can nicely track the trend in the calculated vacancy formation energy. In a similar way, Muñoz-García et al.[6] found that there is a direct relationship between the energetics of vacancy formation in $La_{1-x}Sr_xMO_3$ (M = Mn and Fe) and the extent to which the electrons left behind upon oxygen removal are delocalized onto the oxygen sublattice. In addition, Lee et al.[15] and Chen et al.[16] suggested that a more negative O *p*-band energy should give rise to a stronger transition metal-oxygen bond in the mixed oxides. However, although a reasonable explanation has been given by invoking a rigid band model, the relations established in their work are not satisfactorily linear. Likewise, various structural, energetic, electronic properties have been proposed to explain the trend in the oxygen migration barrier in perovskites, including Kilner critical radius[17], lattice free volume[18], Goldschmidt tolerance factor[18], crystal structure ideality[19], the percentage change in the area of the "critical triangle"[20-21], bulk oxygen *p*-band center[22], the charge transfer between oxygen and transition metal[23], and the change in the magnetic moment of the "central" transition metal ion[24]. Unfortunately, there are also no general rules based on simple physical properties that can guide us in predicting the migration barrier.

Many of the early studies of perovskites were motivated by the desire to develop more efficient MIEC materials and therefore focused only on $LaMO_3$ (M = Mn, Fe, and Co) and their derivatives. As a consequence, a full picture of how the oxygen transport property of metal oxides can be tuned by adjusting composition and structure has not yet been achieved. An eloquent way to gain a broader understanding of this link is to recognize a general pattern of the oxygen mobility in a class of perovskites. In this contribution, DFT+U calculations are first used to calculate the oxygen vacancy formation energies in the La-based perovskites that involve the first series of *d*-block transition metals ($LaMO_3$, M = Sc - Cu), and the effects of the crystal structure and the exchange-correlation functional used have been explored. Next, population analysis and energy decomposition are conducted to identify the dominant factor that determines the reducibility of the $LaMO_3$ perovskites. The oxygen migration barriers for all the possible elementary steps and pathways are then obtained by finding the minimum energy paths (MEPs). After that, the Bader charge analysis is employed to explain the sharp decrease in the migration barrier on moving from $LaCrO_3$ to $LaMnO_3$. Finally, we conclude by identifying the descriptor and electronic origin that can be used to describe the trend in the oxygen bulk diffusion kinetics in perovskites.

2. Computational details

2.1 DFT calculation

All self-consistent DFT calculations have been carried out using the VASP code[25-27], in which the electronic wavefunction at each *k*-point is written as a product of a wave-like part and a cell periodic part, with the latter expanded in terms of a plane wave basis set. The projector-augmented wave (PAW) method[28] was employed to represent the interactions between ion cores and valence electrons, and for the relatively "hard" PAW potentials (as summarized in Table S1 for La, O, and transition metals) a plane wave energy cutoff of up to 600 eV was necessary to converge the total energy *per* atom in $LaMO_3$ to within 1 meV.

The exchange and correlation of the Kohn-Sham theory was treated by using both the recently developed Bayesian error estimation functional with van der Waals correlation (BEEF-vdW)[29] and the Perdew-Burke-Ernzerhof (PBE) functional[30]. It was found that the PBE functional fails to account for the long-range geometrical distortions present in perovskites[31]. In the BEEF-vdW functional, a linear combination of local (Perdew-Wang LDA)[32], semi-local (PBE)[30], and nonlocal correlation (vdW-DF2)[33] is taken as the correlation model space, so that long-range van der Waals interactions and short-range covalent bonding can be simultaneously described with reasonable accuracy, making it an excellent density functional for studies in heterogeneous catalysis and surface science. From this point of view, use of the BEEF-vdW functional could also be a first test for our future work regarding the redox reactions catalyzed by perovskites. The application of the PBE+U method was to compare the results obtained in this work with previously published theoretical

data, as PBE is by far the most widely used functional in representing the structures and energetics of perovskites.

Because standard exchange-correlation functionals suffer from excessive electron delocalization which is connected with the spurious interaction of an electron with itself (previously known as the "self-interaction error")[34], an additional Hubbard-type term was applied in the simplified (rotationally invariant) DFT+U method[35-37] to address the on-site Coulomb interactions between the strongly correlated transition metals *d* states. In practice, an effective interaction parameter U_{eff} was introduced by adding a penalty function to the total energy expression in GGA. The U_{eff} values given in Table S1 were obtained by fitting the calculated thermodynamic quantities to available experimental data, in much the same way as that proposed by Wang et al.[38] and Jain et al.[39] A comparative study performed by Pavone et al. indicated that the application of a higher level of theory (e.g., the HSE hybrid functional) does not offer a significant advantage in terms of the agreement of the calculated oxygen vacancy formation energies with experiment[14]. On the other hand, by summarizing the calculated electronic and magnetic structures of $LaCoO_3$ in earlier theoretical calculations, Ritzmann et al. suggested that DFT+U calculations could reach contradictory conclusions with different choices of the U_{eff} value[40]. Thus, we performed additional calculations to ensure that the used U_{eff} values can correctly reproduce other physical properties of perovskites, such as energy gap and magnetic moment. The details of the derivation and validation of the U_{eff} values are given in Figs. S1 - S3.

Sampling of the Brillouin zone was performed with the Monkhorst-Pack method[41] and electronic occupancies were determined by the Gaussian scheme with an energy smearing of 0.1 eV. For the majority of this study, spin polarization was taken into account to obtain reasonably accurate structures and energetics, where experimentally observed magnetic structures at room temperature were adopted. For example, it was reported that the Co^{3+} cation in $LaCoO_3$ is nonmagnetic (in the low-spin state) below 90 K[42] and becomes paramagnetic with great complexity when temperature is raised. As revealed by X-ray diffraction, soft X-ray absorption, and circular dichroism experiments, Co^{3+} exists either in the intermediate-spin state or as a mixture of cations in the low- and high-spin states[43-44]. Thus, in order to explain the magnetic behavior of $LaCoO_3$ at elevated temperatures, the simple intermediate-spin state that corresponds to a $t_{2g}^5 e_g^1$ electron configuration was adopted by each cobalt ion in the stoichiometric structure. By contrast, the effect of magnetism was not included in the study of $LaScO_3$ and $LaCuO_3$ because preliminary calculations indicated that the introduction of spin polarization has a negligible effect on their structural and energetic properties. The detailed magnetic structures of $LaMO_3$ (M = Sc - Cu) are given in Table S1.

Geometry optimization of the bulk structures of the stoichiometric perovskites was first conducted by using a quasi-Newton algorithm, with both lattice vectors and atomic coordinates allowed to fully relax. The calculated equilibrium lattice constants were then kept fixed and applied in energy minimization of the oxygen-deficient perovskites. The climbing-image nudged elastic band (CI-NEB) method[45-46] was used to find the minimum energy path (MEP) for oxygen ion migration between energetically favorable oxygen vacancies, where a certain number of intermediate images were created and optimized by using a force-based conjugate-gradient method[47]. Both geometry optimization and transition-state search were considered to be converged when the forces on each atom were less than 0.03 eV/ Å.

The mass-weighted Hessian matrix was calculated under the finite difference approximation and diagonalized to give the vibrational frequencies of normal nodes. Then, the enthalpy and Gibbs free energy of molecular O_2 at temperature *T* and pressure *P* were calculated in the ideal-gas limit:

$$H_{O_2}(T,P) = E_{total,O_2} + E_{ZPE} + \Delta H^\circ(0 \to T) \quad (1)$$

$$G_{O_2}(T,P) = H_{O_2} - T \cdot S(T,P) = H_{O_2} - T \cdot S^\circ(T,P) + RT \ln\left(\frac{P}{P^\circ}\right) \quad (2)$$

where E_{total,O_2} is the total energy of molecular O_2 as determined by DFT calculations. E_{ZPE} is the zero-point energy, and $\Delta H^\circ(0 \to T)$ is the enthalpy change from 0 K to temperature *T*. As for the perovskite crystal structures, all degrees of freedom of selected ions were treated in the harmonic limit and the Gibbs free energy can therefore be written as

$$G_{perovskite}(T,P) = E_{total,perovskite} + E_{ZPE} + \Delta U^\circ(0 \to T) - T \cdot S^\circ(T) \quad (3)$$

where $\Delta U^\circ(0 \to T)$ is the change in internal energy from 0 K to temperature *T*. A more detailed derivation of the thermodynamic properties can be found in our previous work[48].

2.2 Structural model

The microstructures of perovskites can be represented as a three-dimensional framework of corner-sharing MO_6 octahedra, with the A-site cations centered in the cub-octahedral cavities of the MO_6 arrangement. The Goldschmidt tolerance factor (t) has conventionally been used to assess the stability and distortion of the perovskite structures, which is defined as

$$t = \frac{r_A + r_O}{\sqrt{2} \cdot (r_M + r_O)} \quad (4)$$

where r_A, r_M, and r_O are the ionic radii of the A-site cation, M-site cation, and O anion, respectively. This geometrical relationship is unity for ideal cubic perovskites with the $Pm\bar{3}m$ space group symmetry but can vary broadly from 0.71 to 1.13 while retaining a stable distorted structure[1, 3]. In general, deviations from the ideal cubic structure can often be traced to the inherent ability of the octahedra to undergo cooperative tiltings in response to the size mismatch between the A and M cations[49-50] and to the local geometrical distortion within the octahedra that removes the e_g- and/or t_{2g}-orbital degeneracy under the influence of an octahedral crystal field[51-52]. The octahedral rotation is commonly referred to as $GdFeO_3$-type distortion (or simply GFO distortion) and would considerably decrease the M-O-M bond angles from 180°, while the internal distortion of the octahedra originates from the Jahn-Teller effect, which is driven by the desire to stabilize the system by lowering the electrostatic repulsion between the transition metal *d* state and the unshared electron pair on the O ion.

Structural determinations carried out at room temperature suggested that there are multiple ways in which the octahedra can tilt[53-54]. Very often perovskites would undergo an $a^-a^-a^-$ or an $a^-b^+a^-$ octahedral tilting distortion (in the Glazer notation[49]), with the symmetry reducing from cubic to rhombohedral or to orthorhombic. In this work, calculations were carried out on La-based perovskites, including all ternary 3*d*-block transition-metal oxides except $LaZnO_3$. The reason $LaZnO_3$ was not under consideration is that the contraction of the 3*d* orbital becomes more pronounced from left to right across the first transition-metal series, making it impossible to remove electrons from the 3*d* orbitals of Zn to form stable Zn^{3+} cations[55]. One can see from Table S1 that the symmetry of the $LaMO_3$ perovskites at room temperature may be correctly described in the space groups *Pbnm* (M = Sc - Fe) and $R\bar{3}c$ (M = Co - Cu). Using this structural information, the bulk structures of the orthorhombic and rhombohedral perovskites were represented as a 2 × 2 × 1 and a 2 × 2 × 2 replication of their respective primitive cells, each containing a total of 80 atoms and 16 formula units. Supercells of this size are highly desired so as to minimize image-image interactions, only a portion of which is shown schematically in Fig. 1a and 1b for clarity. The Brillouin zone of the orthorhombic and rhombohedral structures was sampled with a gamma-centered 3 × 3 × 5 and a gamma-centered 3 × 3 × 3 Monkhorst-Pack grid, respectively.

Apart from the aforementioned low-temperature structures, it was reported that under the SOFC operating conditions (~700 - 1200 K), the thermal vibrations in perovskites would average out the Jahn-Teller distortion and the crystal structures appear to be cubic. The reasoning behind this remark is that the SOFC operating temperature is generally higher than the Jahn-Teller order/disorder transition temperature of perovskites[56-57]. However, despite having the overall cubic symmetry, perovskites are likely to remain distorted in local structures. Not only the GFO distortion but the Jahn-Teller distortion may persist at high temperatures[58-59]. To examine the effect of the perovskite crystal structure on the energetics of oxygen vacancy formation and oxygen ion migration, a 2 × 2 × 2 replication of the ideal cubic unit cell that comprises 40 atoms and 8 formula units was constructed for each $LaMO_3$, the Brillouin zone of which was sampled with a gamma-centered 3 × 3 × 3 *k*-point grid. Distorted structures were obtained by imposing an $a^-b^+a^-$ or an $a^-a^-a^-$ octahedral tilting distortions on the cubic supercells and allowing for internal atomic relaxation. The equilibrium supercell parameters of the pseudocubic structures were obtained by first performing a series of constant-

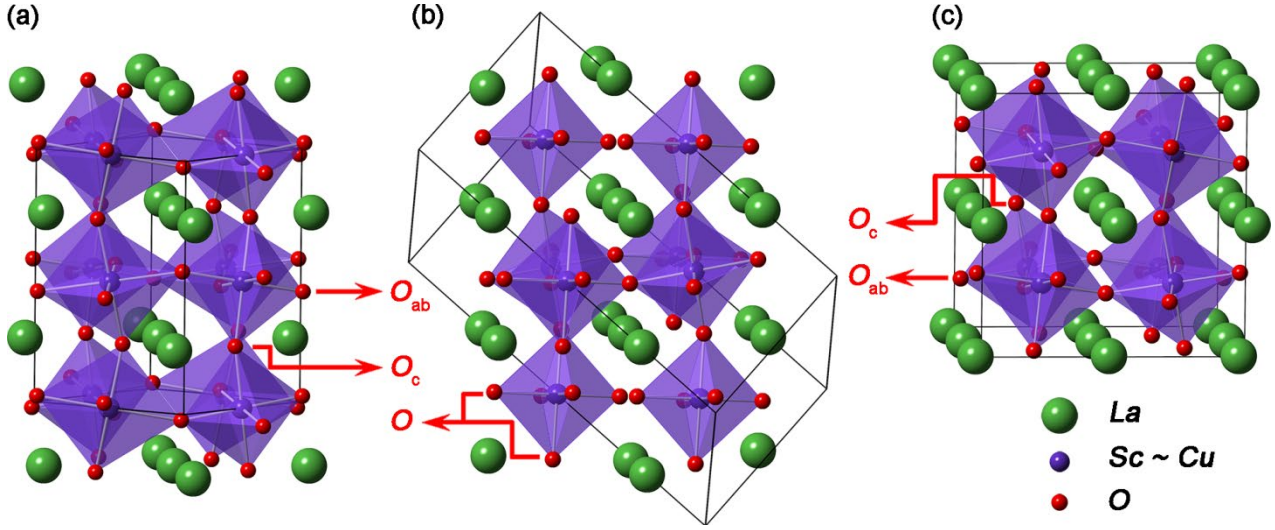

Figure 1. Schematic representations of $LaMO_3$ perovskite structures adopting (a) an orthorhombic, (b) a rhombohedral, and (c) a pseudocubic symmetry.

volume calculations and then fitting the energy *vs*. volume data to the Murnaghan equation of state[60] (see the Supporting Information for details). Our calculated results indicate that the pseudocubic model in the $a^-b^+a^-$ tilt system is energetically more favorable than that in the $a^-a^-a^-$ tilt system. Thus, unless otherwise noted, the $a^-b^+a^-$ octahedral tilting distortion was adopted by all the pseudocubic structures of La-based perovskites.

3. Results and discussion

3.1 Oxygen vacancy formation in $LaMO_3$

3.1.1 Contributions to oxygen vacancy formation energy

Perovskites could be either oxidized or reduced in redox reactions, depending on the reactive gas atmosphere and the oxidation state of the transition metals involved. It is generally accepted that the perovskite-catalyzed redox reactions occur by the Mars van Krevelen mechanism[61]. In the redox cycle, O atoms on the oxide are first transferred to the reducing agents, leaving the surface with oxygen vacancies and transition metal ions in lower oxidation states. When applied in an oxidizing atmosphere, the oxygen vacancies would be attacked by the oxidant molecules that dissociate, followed by the incorporation of the resultant oxygen atoms into the defective surface, thus reforming the catalyst. During the course of the chemical transformation, oxygen concentration gradient is repeatedly established across catalyst nanoparticles and serves as the driving force for oxygen ion transport between bulk oxide and oxide surface.

There are mainly three mechanisms by which the defect migration may occur in crystalline solids, including the vacancy, interstitial, and collinear (or non-collinear) interstitialcy mechanisms. Of them, the vacancy-mediated diffusion mechanism should dominate in most close-packed crystal structures. Indeed, this is the case for oxygen diffusion in bulk perovskite[62-64], where there is no significant difference in ionic radius between the M-site cation and oxygen anion (e.g., 0.785 Å for high-spin Fe^{3+} and 1.26 Å for O^{2-}). Hence, formation of vacancies is essential to oxygen ion migration in perovskites and the detailed knowledge of how readily the M-O-M bond can be broken would lead to a better understanding of the kinetics of the oxygen transport process.

The oxygen vacancy formation energy ($\Delta E_{f,vac}$) in $LaMO_3$ can be calculated as

$$\Delta E_{f,vac} = E_{defective} + \frac{1}{2}E_{O_2} - E_{perfect} \quad (5)$$

where $E_{perfect}$ and $E_{defective}$ are the total energies of the stoichiometric $LaMO_3$ and the defective $LaMO_3$ upon removal of a neutral oxygen atom from the lattice, respectively, and E_{O_2} is the total energy of an O_2 molecule in its triplet state. Under this definition, the formation energy provides a measure of the reducibility of the $LaMO_3$ perovskites, in the sense that the less positive the $\Delta E_{f,vac}$ value, the less is the energy needed to form an oxygen vacancy, and hence the more readily can the transition-metal cations be reduced. Because LDA and GGA generally overestimate the binding strength in the molecular O_2, the O_2 total energy was corrected by fitting the enthalpy and Gibbs free energy of formation of nontransition-metal oxides to experimental values. For the PBE+U and BEEF-vdW+U methods, the resultant formation energies have been increased by 0.42 eV and 0.23 eV *per* oxygen vacancy in $LaMO_3$ (M = Sc, Ti, Cr, Mn, Fe, Co, and Ni) and by 0.37 eV and 0.19 eV *per* oxygen vacancy in $LaMO_3$ (M = V and Cu), respectively. The derivation of the energy corrections is included in the Supporting Information.

Unlike the ideal cubic and distorted rhombohedral structures where all the oxygen sites are equivalent, the orthorhombic and pseudocubic perovskites adopt the $a^-b^+a^-$ tilt system and possess oxygen ions/vacancies that can be classified into two categories. The anions/vacancies that are located at the equators of the MO_6 octahedra (i.e., in the *ab*-plane) are denoted O_{ab}/V_{ab} while those sitting at the remaining apices of the octahedra are denoted O_c/V_c,[65-66] as illustrated in Fig. 1. Calculated results indicate that the vacancy formation energies at these sites are virtually the same (the difference is less than 0.1 eV, see Table S2), which implies that the oxygen vacancies are likely to be distributed uniformly in the bulk of various perovskites. Also, it is found that the perovskite crystal structure has a negligible effect on the predicted results, in accord with the observation by Curnan et al. in $SrMnO_3$ and $SrFeO_3$[67].

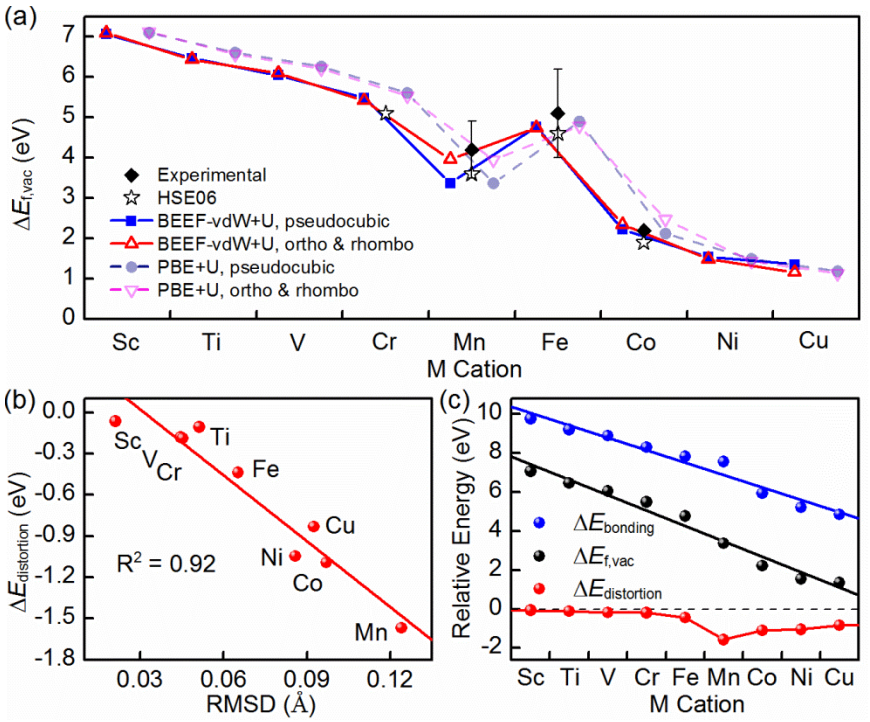

Figure 2. (a). Calculated $\Delta E_{f,vac}$ in $LaMO_3$ by using the BEEF-vdW+U and PBE+U methods. Experimental data reported in ref. 68-70 and theoretical results reported by using the HSE06 hybrid functional in ref. 14 are presented for comparison; (b). linear scaling relations between $\Delta E_{distortion}$ and the RMSD of the ions in the defective structures; (c). decomposition of $\Delta E_{f,vac}$ into $\Delta E_{distortion}$ and $\Delta E_{bonding}$, in which the constituent transition metals are put in order of decreasing the vacancy formation energy.

Fig. 2 shows the calculated oxygen vacancy formation energies in $LaMO_3$ as a function of the atomic number of the constituent transition metals by using the BEEF-vdW+U and PBE+U methods. It can be seen from the figure that our calculated results are in remarkably good agreement with available thermogravimetric data[68-70], even better than is obtained from the HSE06 hybrid functional[14]. The first four $LaMO_3$ (M = Sc - Cr) perovskites have oxygen vacancy formation energies higher than 5.4 eV and can therefore hardly be reduced even under harsh conditions, which explains much of the behavior exhibited by these oxides in redox reactions[71-73]. In general, the perovskites exhibit an increased reducibility as we move from $LaScO_3$ to $LaCuO_3$. However, the oxygen vacancy formation energy in $LaFeO_3$ is exceptionally high (4.7 - 4.9 eV), regardless of the crystal structures adopted and the exchange-correlation functionals used (By using the quantum Monte Carlo method, Santana et al.[74] even obtained a high value of 6.24 eV for $LaFeO_3$). This finding has been verified by previous experimental observations that the Fe-O bond in $LaFeO_3$ is even harder to break than the Mn-O bond in $LaMnO_3$[68-69]. By performing both the GGA+U and hybrid density functional calculations, Pavone et al.[14] and Lee et al.[75] observed a similar trend from $LaCrO_3$ through $LaNiO_3$ and suggested that the overall shape of the curves is a result of two effects: the intrinsic M-O bond strength that decreases on moving across the first transition-metal period and the preference for maximum electron exchange stabilization that causes the non-monotonic behavior. The latter can be rationalized as follows. In the defect-free $LaMO_3$, the high-spin Mn^{3+} and Fe^{3+} cations have a $t_{2g}^3e_g^1$ and a $t_{2g}^3e_g^2$ electron configuration, respectively. When a neutral oxygen atom is removed from the lattice, the two electrons left behind will localize to a large extent on the two M^{3+} cations nearest to the vacancy. For Mn^{3+}, whether the electron goes into a t_{2g} or into an e_g orbital depends on the relative energies of the crystal-field splitting energy and the spin-paring energy. Our calculated results indicate that the high-spin Mn^{2+} that has a half-filled subshell ($t_{2g}^3e_g^2$) is energetically more favorable, which is driven by the desire to maximize the exchange stabilization. By contrast, adding an antiparallel spin to the Fe^{3+} cation may reduce the exchange interaction between the *d* electrons of the same spin and cause them to experience a higher Coulomb repulsion, thus giving rise to a higher energy. Usually the negative of the third ionization energy (IP^{3rd}) is used as a measure of how readily M^{3+} cations can gain an electron. The higher value for Mn^{2+} (33.78 eV) than for Fe^{2+} (30.65 eV) also supports the idea that adding an electron to the Mn^{3+} cation would release more heat.

To understand better the major factor that influences the ease with which the M-O-M bond can be broken, it is advantageous to decompose the $\Delta E_{f,vac}$ into geometrical and electronic contributions:

$$\begin{aligned}\Delta E_{f,vac} &= E_{defective} + \frac{1}{2}E_{O_2} - E_{perfect} \\ &= \left(E_{defective} - E_{defective}^{constrained}\right) + \left(E_{defective}^{constrained} + E_O - E_{perfect}\right) + \left(\frac{1}{2}E_{O_2} - E_O\right) \\ &= \Delta E_{distortion} + \Delta E_{bonding} + \frac{1}{2}\Delta E_{binding,O_2}\end{aligned} \quad (6)$$

where $E_{defective}^{constrained}$ is the single-point energy of the oxygen-deficient $LaMO_3$ without any geometry optimization and

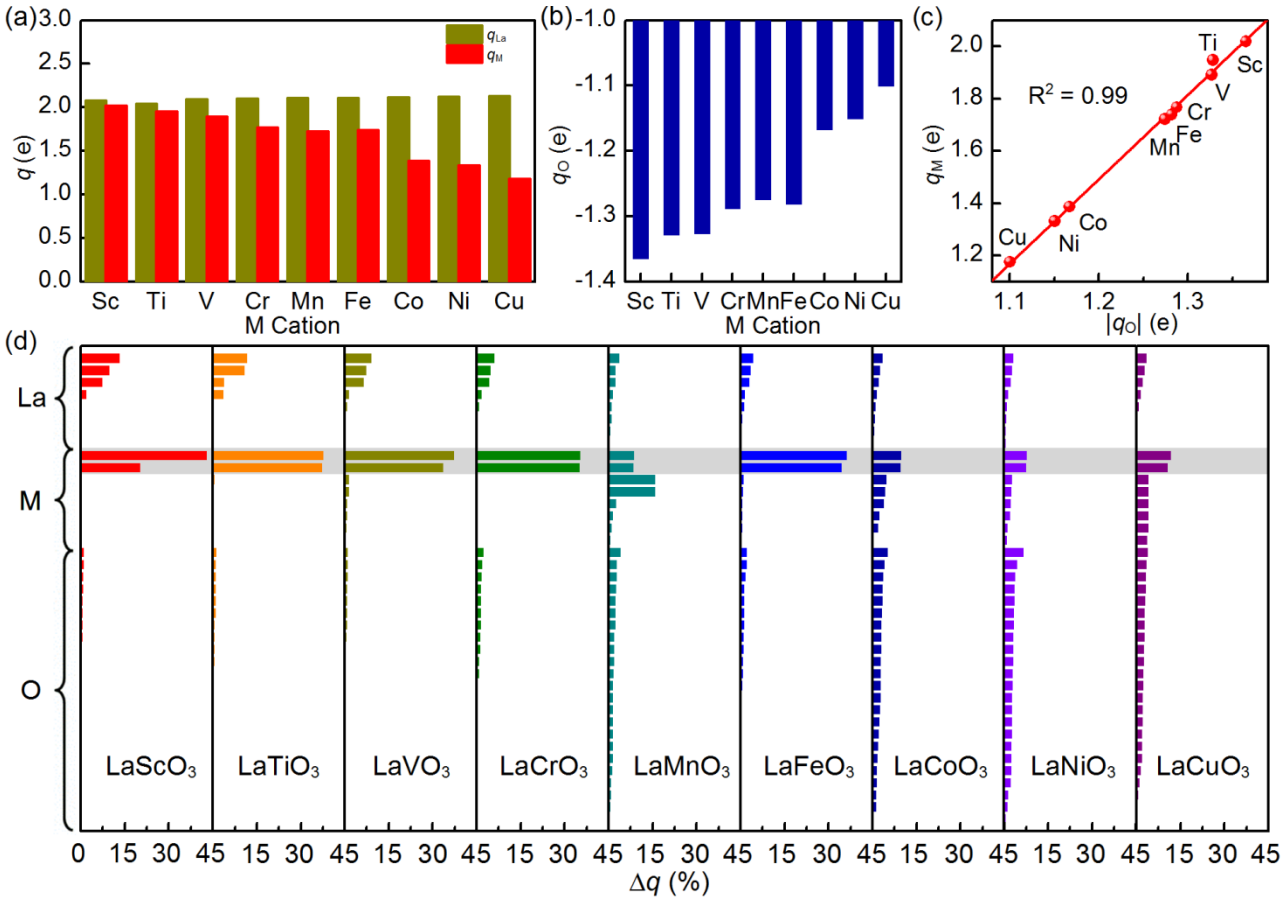

Figure 3. Calculated effective Bader charges on (a) La and M and on (b) O in the pseudocubic $LaMO_3$ by using the BEEF-vdW+U method; (c) linear scaling relation between the partial charges on transition metal and oxygen ions; (d) percentage of the electrons gained by each remaining ion upon oxygen vacancy formation. The data for the nearest-neighbor transition metals of the oxygen vacancy are shaded in gray.

its difference from the $E_{defective}$ naturally defines the distortion energy ($\Delta E_{distortion}$). Since the $\Delta E_{distortion}$ is the relaxation energy of the remaining crystal structure upon removal of an oxygen atom, it is expected to be strongly dependent on the displacement of the ions in the defective structures. Indeed, plotting the $\Delta E_{distortion}$ against the root mean squared displacement (RMSD) of the remaining ions gives a good straight line (see Fig. 2b), meaning that the RMSD can be used to gauge the degree of geometrical distortions arising from the oxygen abstraction. The second contribution to the $\Delta E_{f,vac}$ is the bonding energy ($\Delta E_{bonding}$), which by definition is the energy required to remove an oxygen atom from the fixed oxide lattice and thus provides a measure of the direct interaction between them. Finally, the third term on the right-hand side of Eq. (6), $\Delta E_{binding,O_2}$, is due to the binding of O atoms in gaseous O_2 and keeps constant in the calculation of the $\Delta E_{f,vac}$ in the different perovskites. Fig. 2c shows the calculated $\Delta E_{f,vac}$, $\Delta E_{bonding}$, and $\Delta E_{distortion}$ plotted against the perovskite materials, in which the constituent transition metals are put in order of decreasing the vacancy formation energy. From the figure, one can see that although the two straight lines have slightly different slopes, the $\Delta E_{f,vac}$ and $\Delta E_{bonding}$ apparently follow the same trend; that is, the variation of the oxygen vacancy formation energy is determined largely by the change in the bonding energy.

3.1.2 Electronic structure analysis

Population analysis methods partition the electron density between nuclei so that a number of electrons can be assigned to each nucleus. Armed with this knowledge, we can examine more closely the nature of the chemical bonds between La, M, and O in the $LaMO_3$ perovskites and gain deeper insight into the interactions responsible for the bonding between ions of unlike charge in transition-metal oxides. Here the Bader charge analysis, which is based on the concept of a gradient vector path, was performed to keep track of the charge redistribution upon formation of an oxygen vacancy in $LaMO_3$. As indicated in Fig. 3a and 3b, the calculated effective Bader charges on La (q_{La}), M (q_M), and O (q_O) in the stoichiometric structures are either less positive or less negative than their respective formal oxidation states, implying that the chemical bonding in the perovskites could be characterized as ionic with some covalent character. Moreover, the M-O bond is less polar than the La-O bond in light of the fact that the La cations carry more partial positive charges. Going from $LaScO_3$ to $LaCuO_3$, the oxidation state of La keeps nearly constant (+2.04 - +2.13), whereas the M and O ions become less positively and negatively charged,

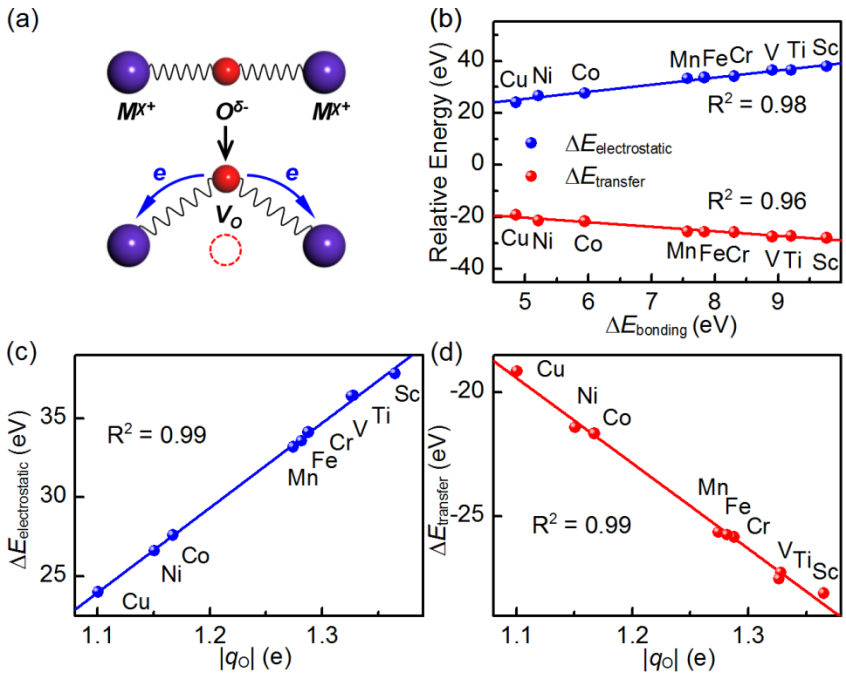

Figure 4. (a). Illustration of removal of an oxygen atom from fixed oxide lattice; (b). decomposition of $\Delta E_{bonding}$ into $\Delta E_{electrostatic}$ and $\Delta E_{transfer}$; (c). linear scaling relation between $\Delta E_{electrostatic}$ and the actual partial charge on oxygen; and (d). linear scaling relation between $\Delta E_{transfer}$ and the actual partial charge on oxygen. The calculated results are obtained in the pseudocubic structure by using the BEEF-vdW+U method.

respectively, except that the Fe-O bond is more polar than the Mn-O bond. Interestingly, the charges on the M and O ions scale linearly with each other (see Fig. 3c), which well represents the varying degree of electron density shift in these substances.

Upon removal of a neutral oxygen atom, a certain number of electrons (~1.10 - 1.37 e) are left behind and will be transferred to the defective $LaMO_3$. The percentage of the electrons gained by each remaining ion is given in Fig. 3d. From the figure, one can see that the electrons left behind would delocalize over the whole oxide lattice. However, the largest number of electrons will be localized on the transition metals that are nearest to the oxygen vacancy (the corresponding data are shaded in gray in the figure). The only exception occurs in $LaMnO_3$, where the two next-nearest neighbor Mn cations gain the most electrons. This phenomenon can be explained by the so-called superexchange interaction[76], in which the hopping of d electrons from the Mn^{2+} to the Mn^{3+} cation occurs via the p states of the shared oxygen ions, leading to the superexchange between these cations.

If we add up the percentages for each element in each oxide, it is interesting to find that, for the $LaMO_3$ (M = Sc, Ti, V, Cr, and Fe) perovskites, only less than 13 % of the electrons left behind are delocalized onto the oxygen sublattice, while in $LaMO_3$ (M = Mn, Co, Ni, and Cu) that have a lower vacancy formation energy, more than 36 % of the electrons would be withdrawn by the oxygen ions. The results obtained from the orthorhombic and rhombohedral structures as well as the PBE+U method are found to follow the same trend (see the Supporting Information for details). The oxygen vacancy formation in $La_{1-x}Sr_xMO_3$ (M = Mn and Fe) has previously been investigated by Muñoz-García et al.[24], who claimed that ~20 % of the extra charge would go into the oxygen sublattice after removing an oxygen atom from $LaFeO_3$. When Sr was substituted for 50 % of the La cations, roughly 80 % of the electrons were delocalized onto the remaining oxygen ions and no local reduction of Fe was observed. They suggested that the lower oxygen vacancy formation energy in $La_{0.5}Sr_{0.5}FeO_3$ is due to the higher degree of charge delocalization, which minimizes the repulsion arising from the defect formation. Thus, it appears as if the degree of electron delocalization onto the oxygen lattice would determine how much the oxygen-deficient perovskites can be stabilized.

3.1.3 Contributions to bonding energy

For the purposes of exploring how the charge redistribution may affect the energetics of vacancy formation, we need to further separate different contributions to the $\Delta E_{bonding}$. On the basis of the information given by the electronic structure analysis, oxygen vacancy formation can be envisioned as occurring in three steps: (1). M-O-M bond cleavage giving rise to infinitely widely separated $O^{\delta-}$ and positively charged defective $LaMO_3$; (2). loss of electrons from $O^{\delta-}$ to form an O atom; and (3). gain of electrons by the oxygen-deficient structure, as illustrated in Fig. 4a. Of the three steps, the last two can be combined into one single step to describe the electron transfer from $O^{\delta-}$ to the defective $LaMO_3$. Accordingly, the bonding energy is divided into two terms:

$$\Delta E_{bonding} = \Delta E_{electrostatic} + \Delta E_{transfer} \quad (7)$$

where $\Delta E_{electrostatic}$ is the change in the electrostatic potential energy of interaction between oxygen and the remaining fixed oxide lattice and $\Delta E_{transfer}$ is the energy change associated with the electron transfer from $O^{\delta-}$ to the remaining ions.

Each O ion in $LaMO_3$ experiences not only electrostatic attractions from the oppositely charged cations but also repulsions from all the other like-charged anions. The coulomb potential energy of an O ion ($E_{electrostatic}$) is the sum of all the electrostatic contributions and can therefore be used to measure the strength of ionic bonding in the stoichiometric perovskites. Here the quantity $E_{electrostatic}$ was calculated by using the EUGEN code[77], on the assumption that the ions involved in $LaMO_3$ behave as positive and negative points of charge separated by interatomic distances:

$$E_{electrostatic} = M_O \times \frac{z_O \cdot e^2}{4\pi\varepsilon_0 r_0} \quad (8)$$

where z_O is the electrical charges on the O ion, r_0 is the nearest neighbor distance, and M_O is the Madelung constant of the O ion that can be written as

$$M_O = \sum_i \frac{z_i}{r_{iO} / r_0} \quad (9)$$

where z_i is the electrical charges on the *i*th ion and r_{iO} is the interatomic distance between the *i*th ion and the O ion.

Fig. 4b shows the calculated $\Delta E_{electrostatic}$ and $\Delta E_{transfer}$ plotted against the $\Delta E_{bonding}$. From the figure, one can see that the $\Delta E_{electrostatic}$ is much more positive than the bonding energy and increases linearly with it. On the other hand, since the $\Delta E_{electrostatic}$ is intimately related to the charge on the oxygen ion in the stoichiometric $LaMO_3$, it is not surprising to learn that the scaling between these two quantities also gives a straight line (see Fig. 4c). The large positive values for the energy change signify that the O ions interact strongly with the cations in the tightly bonded solids. In contrast, the energy change associated with the electron transfer takes negative values and becomes more negative as the bonding energy rises, which means the energy released by adding electrons to the oxygen-deficient crystal structure more than makes up for the endothermic nature of removing electrons from $O^{\delta-}$ to form an O atom, making the overall electron transfer an exothermic process.

It is important to note that $LaFeO_3$ has a more negative $\Delta E_{transfer}$ value than $LaMnO_3$; that is, $LaFeO_3$ has its defective structure stabilized more significantly by the electron transfer, although the electrons left behind upon oxygen removal are delocalized to a smaller extent onto the remaining oxygen ions (see Fig. 3d). As shown in Fig. 4d, however, a very good linear scaling relation is established between the $\Delta E_{transfer}$ and q_O, which demonstrates that the energy change associated with the electron transfer is determined dominantly by the number of the electrons left behind upon formation of oxygen vacancy, rather than by the degree of electron delocalization onto the oxygen sublattice. Furthermore, given the fact that the charges on the transition metal and the oxygen ion scale with each other, either of them can be used to explain the trend in the $\Delta E_{electrostatic}$ and $\Delta E_{transfer}$, and hence in the $\Delta E_{bonding}$ and $\Delta E_{f,vac}$.

3.2 Oxygen migration in $LaMO_3$

3.2.1 Oxygen migration elementary steps

When oxygen concentration gradients are established in the bulk, the hopping of ions and vacancies takes place in opposite directions and at the same rate, both following the vacancy-mediated diffusion mechanism. The energy decomposition and electronic structure analysis given above clearly indicate that, the less the electrical charges carried by the transition metal and oxygen ions, the more readily can oxygen vacancies be formed in $LaMO_3$. Hence, of particular interest is how the geometric and electronic structures of perovskites would affect the energy barriers for oxygen bulk diffusion.

Considering the high symmetry the rhombohedral structure adopts, there exist only two possible elementary

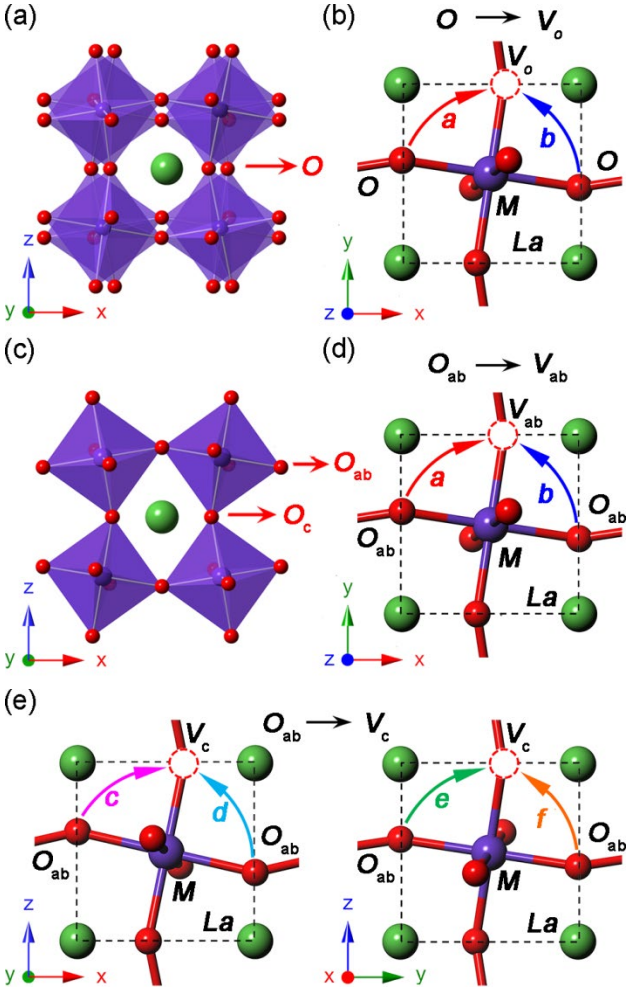

Figure 5. Schematic representations of (a) distorted local structures and (b) two oxygen migration elementary steps in the rhombohedral $LaMO_3$; and schematic representations of (c) distorted local structures and (d-e) six oxygen migration elementary steps in the pseudocubic and orthorhombic $LaMO_3$.

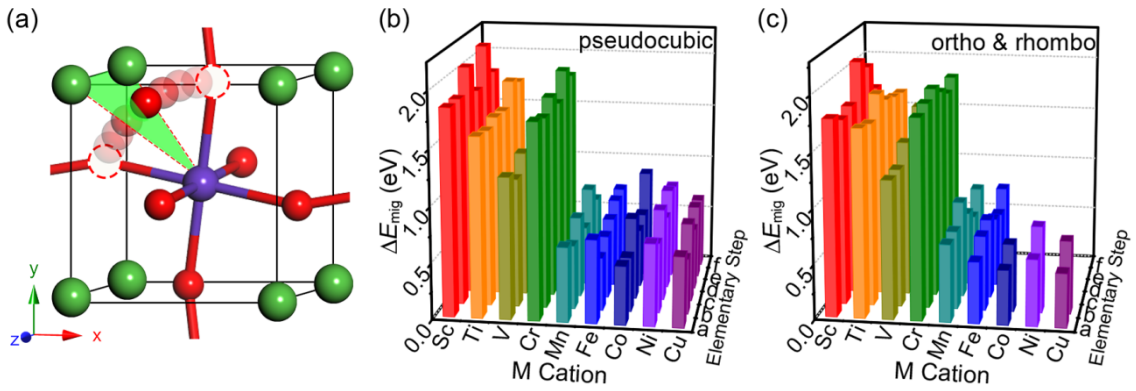

Figure 6. (a) Illustration of the two-dimensional curved pathway for oxygen migration; calculated energy barriers (ΔE_{mig}) for oxygen migration elementary steps in the (b) pseudocubic and (c) orthorhombic & rhombohedral $LaMO_3$ (M = Sc ~ Cu) by using the BEEF-vdW+U method.

steps (steps *a* and *b*) for oxygen to migrate between equivalent vacancies, as illustrated in Fig. 5a and 5b. The reason the two migration steps are inequivalent is because the O-B-O bond angles are distorted by the Jahn-Teller effect and hence deviate from the ideal value of 90 °. As for the pseudocubic and orthorhombic $LaMO_3$, however, the situation becomes much more complicated. When viewed along the three crystallographic axes, the crystal structures have two distinguishable migration steps in each of the planes perpendicular to the axes, which gives totally six elementary steps for each substance (see steps *a* - *f* in Fig. 5c-5e). It is worth noting that, unlike in the two V_{ab}-V_{ab} and the four V_{ab}-V_c migration steps, the direct oxygen hopping between two V_c sites is unlikely to occur, owing to the long distance that needs to be travelled and the hindering presence of the large La ions.

The MEPs for oxygen ion migration between energetically favorable oxygen vacancies were found by using the CI-NEB method. As can be seen from Fig. 6a, the oxygen migration proceeds along a two-dimensional curved pathway that is away from the edge of the MO_6 octahedron, in accord with the predictions made by Jones and Islam in $LaFeO_3$[65] and by Zhang in $SrTiO_3$[78]. During the course of the process, the hopping O ion passes through the opening of a triangle defined by two La and one M cations, and in the transition state this triangle is located slightly below the migrating O ion when viewed in the opposite direction of the corresponding octahedral rotation (e.g., the clockwise octahedral rotation about the *z* axis in Fig. 6a), which causes the three cations to move outward, so reducing the repulsive interactions.

The calculated energy barriers for the elementary steps in both the pseudocubic and the orthorhombic & rhombohedral perovskites are presented in Fig 6b and 6c. From the figure, one can see that the migration barriers in each $LaMO_3$ vary from step to step and the energy difference spans the range of 0 - 0.4 eV, suggesting that the local geometrical distortion has a considerable effect on the oxygen transport behavior. In $LaMnO_3$, for example, significant bulk reconstruction may occur in response to the oxygen migration, and a longer distance over which the ions are transported and displaced tends to give rise to a higher energy barrier (see the energy profiles in Fig. S8 and S9). On the other hand, comparison between Fig. 6b and Fig. 6c reveals that the GFO distortion plays a minor role in determining the activation energy for the migration steps. The changes in the direction and magnitude of the octahedral tilting can only alter the estimated barriers by less than 0.2 eV. If we collect the lowest oxygen migration barrier in each $LaMO_3$, we find that the values for the first four perovskites vary from 1.2 eV to 1.9 eV while those for the later five materials are much lower and lie between 0.4 and 0.7 eV, regardless of the exchange-correlation functional used (see Fig. S10 for the data obtained by using the PBE+U method).

3.2.2 Oxygen diffusion pathways

In many of the practical applications of perovskites, the mixed oxides serve as oxygen carrier and/or catalyst. Both the reduction and reoxidation of oxide nanoparticles are required to occur at a reasonable rate. In particular, to achieve rapid exchange between lattice and surface oxygen and facile incorporation of oxygen into the solid from the gas phase, oxygen ions would have to pass through the whole perovskite nanoparticle along the pathways that are kinetically most favorable. Although many theoretical efforts have been made to estimate the energy barriers for oxygen migration elementary steps in $LaMO_3$[6, 22-24], none of them have been focused on the ionic conductivity along specific pathways.

For long-range oxygen transport to occur in the pseudocubic and orthorhombic $LaMO_3$, the six migration elementary steps can be combined into six diffusion pathways, three in the *xy*-plane (commonly referred to as "in-plane" pathways[79-80]) and the other three in the *xz*- or *yz*-plane (called "out-of-plane" pathways), as shown schematically in Fig. 7a. In each unit cell, the diffusion pathways are depicted as a combination of elementary steps. For example, PATH(I) is essentially step *a* repeating along the diagonal of the *xy*-plane, and PATH(VI) is composed of steps *c*, *d*, *e*, and *f* connected in series and along the diagonal of the *xz*-plane. Similarly, there exist three possible pathways for oxygen to diffuse in the rhombohedral structures, as illustrated in Fig. 7b. Of them, PATH(I) and PATH(II) are extended along and perpendicular to the

cell edge, respectively, and PATH(III) is along the cell diagonal, consisting of interconnected steps *a* and *b*.

Table 1 presents the calculated energy barriers for the kinetically most favorable oxygen diffusion pathways in the pseudocubic and orthorhombic & rhombohedral perovskites (The data sets for the other pathways are included in Supporting Information). One can see from the table that PATH(II) has the lowest oxygen diffusion barriers in all the pseudocubic structures. Taking $LaFeO_3$ as an example, we plot the MEPs for the six diffusion pathways in Fig. 7c. Comparison between the energy barriers points clearly to the anisotropic oxygen diffusion, and reveals that oxygen ions migrate preferentially along the diagonal of the *xy*-plane in $LaFeO_3$. Similarly, in the orthorhombic structures, the *xy*-plane is also preferred by the migrating oxygen, and the only difference is that $LaMO_3$ (M = V - Fe) favors PATH(I) rather than PATH(II). Experimentally, the effect of the structural dimensionality on the oxygen diffusion behavior in perovskites and related mixed oxides has been examined by using the isotopic exchange technique[81-82]. It has been confirmed that both the tracer diffusion coefficient D^* and the surface exchange coefficient k^* are higher along the *xy*-plane than those in the *z*-axis direction. In the rhombohedral structures, however, the situation is quite different. The data in Table 1 indicate that their capability of reversible oxygen storage is strongly dependent on the kinetics of oxygen diffusion along the cell edge. For example, PATH(I) dominates the oxygen migration in the rhombohedral $LaNiO_3$, as evidenced by the lowest energy barrier among the three pathways in Fig. 7d.

The detailed consideration of all the possible elementary steps and pathways in this work ensures that the lowest energy barriers for oxygen migration are reported, so that the comparison between the calculated and experimental values is straightforward. As far as the most widely studied $LaMO_3$ (M = Mn - Ni) compounds are concerned, our calculated results agree satisfactorily with the available experimental values (0.73 eV for $LaMnO_3$[83], 0.77 ± 0.25 eV for $LaFeO_3$[62], and 0.58 eV for $LaCoO_3$[84]), and are consistent with the theoretical predictions made by using a Mott-Littleton methodology[85] and a standard DFT method[22]. On the other hand, since the four early transition metal-based $LaMO_3$ (M = Sc - Cr) perovskites are nearly irreducible, little attention has been given to the abrupt decrease in the migration barrier when going from $LaCrO_3$ to $LaMnO_3$ (shown in Fig. 6 and Table 1) and, not surprisingly, there is not uniform agreement on the physical origin of this observation.

3.2.3 The factor determining oxygen migration barriers

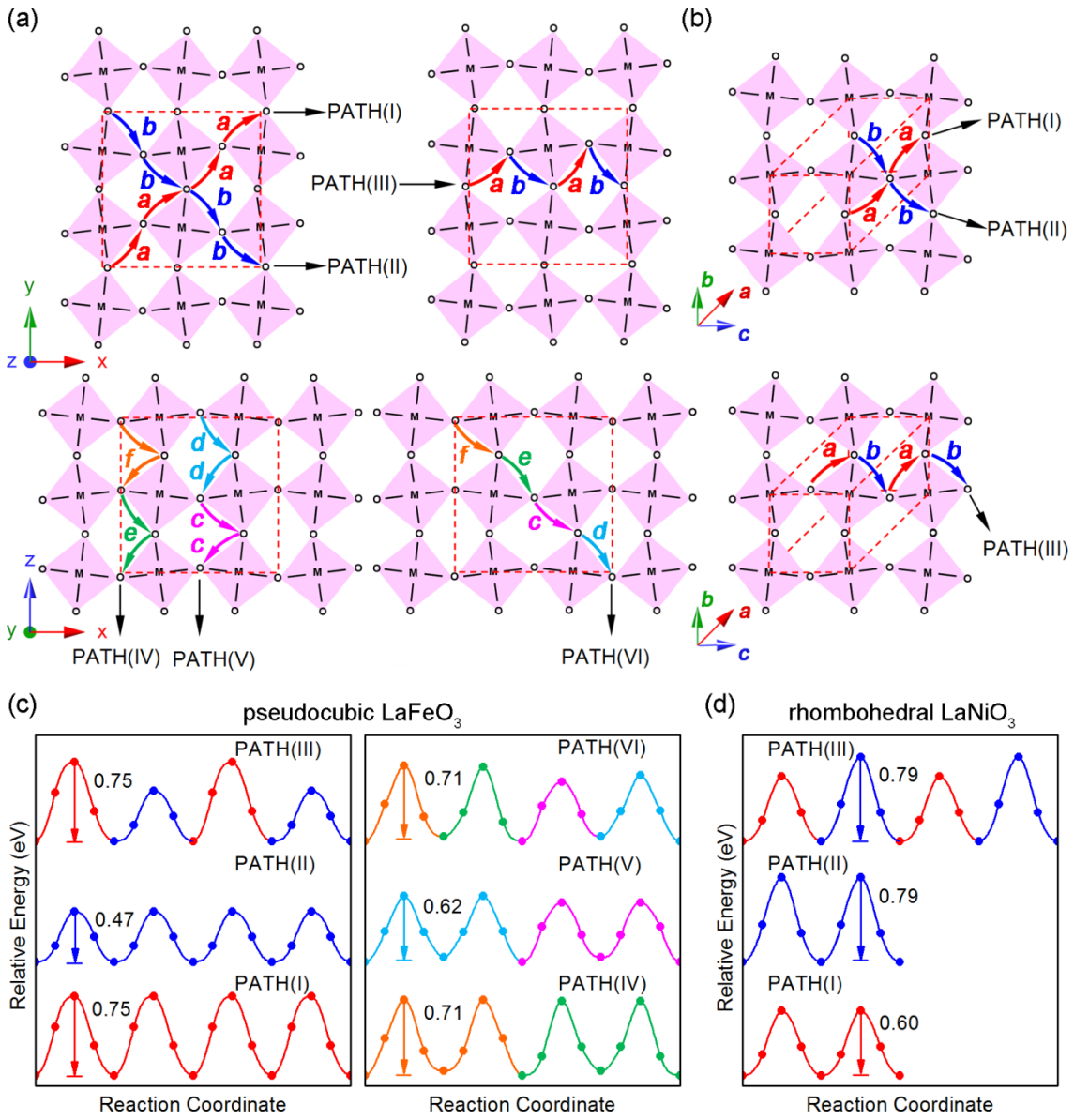

Figure 7. (a) Illustration of six oxygen transport pathways in the pseudocubic and orthorhombic $LaMO_3$; (b) illustration of three oxygen transport pathways in the rhombohedral $LaMO_3$; (c) MEPs for the six oxygen transport pathways in the pseudocubic $LaFeO_3$ obtained by using the BEEF-vdW+U method; (d) MEPs for the three oxygen transport pathways in the rhombohedral $LaNiO_3$ obtained by using the BEEF-vdW+U method.

In early studies, various structural properties have been proposed to explain the trend in the oxygen migration barrier in perovskites. However, none of them show strong correlation with the calculated data. Mayeshiba and Morgan believed that these geometric descriptors could only be effective when looking at fine changes in very similar geometries[22]. As a result, much of the recent research has been directed toward the energetic and electronic properties of perovskites.

A data mining analysis of over 40 perovskites suggested that the systems with low energy barriers generally have low metal-oxygen bond strengths, as measured by oxygen vacancy formation energy and oxygen *p*-band center energy, although neither correlation is particularly strong for materials having moderate barriers[22]. On the contrary, by examining the structure distortion, charge redistribution, and transition state energy, Mastrikov et al.[23] argued that the migration barrier in $(La,Sr)(Co,Fe)O_{3-\delta}$ is determined not by the oxygen vacancy formation energy but by the number of electrons transferred in the transition state between the migrating O and the central M. The underlying reason is that when electrons are transferred from O to M, the size of the oxygen ion becomes smaller, making its passage through the "critical triangle" easier. However, through the use of a PBE+U method, Ritzmann et al.[40] found that there is almost no change in the charge (less than 0.02 e) on the migrating O from the initial state to the transition state for both LS and HS/LS $LaCoO_3$, which cannot explain the difference in the calculated barrier heights. Their electronic structure analysis, on the other hand, revealed that the oxygen mobility is significantly influenced by the spin state of Co^{3+}. Thus, the question that now arises is whether there exists a quantity that can be used to describe the trend in the migration

Table 1. Calculated energy barriers (ΔE_{mig}^{path}) for the kinetically most favorable oxygen diffusion pathways in the pseudocubic and orthorhombic & rhombohedral $LaMO_3$ by using the BEEF-vdW+U method.

Perovskite	Pseudocubic		Ortho & rhomb	
	Favorable pathway	ΔE_{mig}^{path} (eV)	Favorable pathway	ΔE_{mig}^{path} (eV)
$LaScO_3$	II	1.84	II	1.70
$LaTiO_3$	II	1.57	II	1.67
$LaVO_3$	II	1.15	I	1.26
$LaCrO_3$	II	1.70	I	1.82
$LaMnO_3$	II	0.57	I	0.71
$LaFeO_3$	II	0.47	I	0.56
$LaCoO_3$	II	0.49	I	0.50
$LaNiO_3$	II	0.62	I	0.60
$LaCuO_3$	II	0.50	I	0.49

barrier in any perovskite materials, especially for those in the nonmagnetic state.

$LaCrO_3$ and $LaFeO_3$ are two representative perovskites that have high (1.70 eV) and low (0.47 eV) migration barriers, respectively. To study the electron density redistribution upon oxygen migration, two-dimensional slices are displayed along the (002) plane of these two perovskites, showing the charge density difference between the transition and initial state (see Fig. 8a-c). The figure shows clearly that three M cations are involved in the migration process, one coordinated to the hopping O throughout the process (referred to as the central M_A in the figure) and the other two bonded to the hopping O either in the initial state (M_B) or in the final state (M_C). At first glance, the electron density around the cations is significantly redistributed in both the two cases, and the distortion is more pronounced in $LaFeO_3$ than in $LaCrO_3$. However, closer examination of the charge density difference reveals that the distortion is due primarily to the changes in the positions of the ions (The spheres connected by the dotted and solid lines represent the positions of the ions in the initial and transition states, respectively). Hence, in order to obtain a more accurate picture of how electrons are transferred in the systems, we must turn to the local partial charge on each individual ion. The effective Bader charges on the transition metals along the MEPs for oxygen migration in $LaCrO_3$ and $LaFeO_3$ are given in Fig. 8d and 8e, respectively. From the figure, one can see that in both the two perovskites the calculated partial charges on the M_B and M_C cations increase and decrease, respectively, as oxygen migrates toward its adjacent vacancy. An interesting feature of the data is that the total number of electrons gained by the M_B cation equals that lost by the M_C cation, implying that the oxygen migration is accompanied by a simultaneous electron transfer in the opposite direction. By performing DFT+U calculations, Ritzmann et al.[24] observed a similar switch in the magnetic moments on Fe_B and Fe_C during the oxygen migration in $LaFeO_3$, and successfully interpreted the phenomenon in terms of the reduction of Fe_B^{3+} to Fe_B^{2+} and the concurrent oxidation of Fe_C^{2+} to Fe_C^{3+}. The slight difference between the energy profiles for $LaCrO_3$ and $LaFeO_3$ is that the latter adopts a less symmetrical shape, which stems from the fact that the transition state in $LaFeO_3$ more closely resembles its preceding image in the ionic character.

Unlike the M_B and M_C cations, the central M_A in $LaCrO_3$ and $LaFeO_3$ exhibits completely different ionic behaviors. It is clear from Fig. 8d and 8e that the partial charge on Fe_A keeps nearly constant throughout the migration process while that on Cr_A first reaches a maximum as oxygen migrates to the transition state and then falls back to its initial value in the final state. Since the Cr_A cation has at least one vacancy in its vicinity during the process, the electron donation from Cr_A is energetically unfavorable, which is likely responsible for the high migration barrier in $LaCrO_3$. Indeed, comparison of the energetics and electronic structures between $LaCrO_3$ and $LaFeO_3$ definitely demonstrates that a higher degree of charge redistribution on the M_A cation generally results in a higher transition state energy, as is the case observed by Mastrikov et al.[23] in $(La,Sr)(Co,Fe)O_{3-\delta}$ and $(Ba,Sr)(Co,Fe)O_{3-\delta}$.

To verify that this monotonic relationship can be generalized and extended to all the La-based 3*d*-block transition-metal oxides, the changes in the partial charges on the central M_A (q_{M_A}) cations from the initial state to the transition state, together with the oxygen migration barriers, are summarized in Fig. 8f. The calculated results indicate that the oxygen migration in the first four $LaMO_3$ (M = Sc - Cr) perovskites would be kinetically hindered by a dramatic change in the q_{M_A}, although the oxygen migration barrier in $LaVO_3$ is exceptionally low given the fact that the q_{M_A} values in $LaScO_3$, $LaVO_3$, and $LaCrO_3$ are comparable. As stated in the Introduction, some structural properties have previously been proposed to explain the variation in the activation energy for oxygen migration. After analyzing all these quantities, we found that the percentage change in the area of the "critical triangle" from the initial state to the transition state is particular high for $LaVO_3$, which provides a rational interpretation of the low migration barrier therein. For the later five $LaMO_3$ (M = Mn - Cu) materials, it is worth noting that the low and narrowly distributed barrier values cannot be explained by the significant difference in the oxygen formation energy, but rather are directly related to the mi-

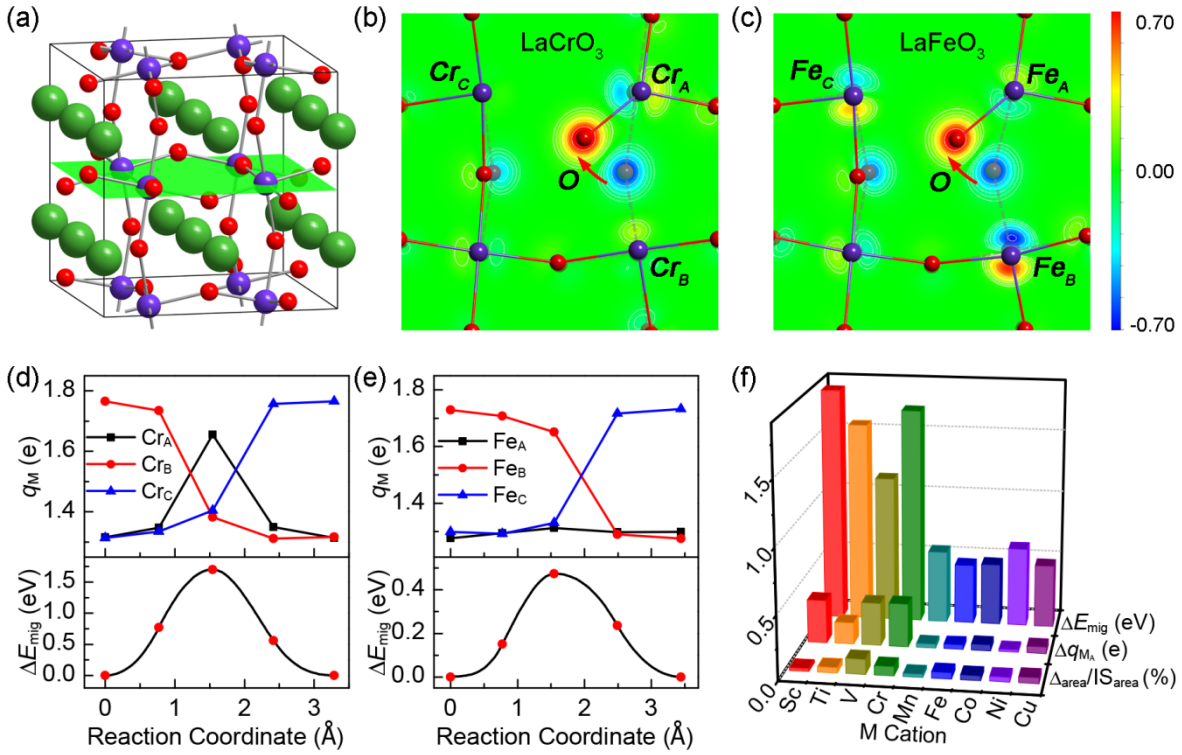

Figure 8. (a) Schematic representation of the (002) plane (shaded in green) in the pseudocubic structure; two-dimensional slices displayed along the (002) plane, showing the charge density difference between the transition and initial state for oxygen migration in (b) $LaCrO_3$ and (c) $LaFeO_3$; (d) effective Bader charges on transition metals along the MEPs for oxygen migration in (d) $LaCrO_3$ and (e) $LaFeO_3$; (f) relationship among the energy barrier for oxygen migration, the change (Δq_{M_A}) in the effective Bader charge on the central M_A cation from the initial state to the transition state, and the percentage change ($\Delta_{area} / IS_{area}$) in the area of the "critical triangle" from the initial state to the transition state.

nor changes of the q_{M_A} (< 0.054 e) in all these perovskites. Therefore, the abrupt decrease in the ΔE_{mig} on going from $LaCrO_3$ to $LaMnO_3$ can be attributed to the different degrees of charge redistribution on the central M_A during the migration process.

3.3 The descriptor of oxygen transport kinetics in perovskites

Having obtained the oxygen vacancy formation energies and oxygen migration barriers in $LaMO_3$, we are now in a position to identify the descriptor that can be used to describe the kinetics of the oxygen bulk transport process. In the vacancy-mediated diffusion mechanism, if the transport is due to discrete hops of oxygen ions, the oxygen diffusion coefficient (D_{oxygen}) can be expressed as

$$D_{oxygen} = \frac{C_{vac}}{C_{oxygen}} D_{vac} = \frac{C_{vac}}{3 - C_{vac}} D_{vac} \qquad (10)$$

where D_{vac} is the vacancy diffusion coefficient, C_{vac} and C_{oxygen} are the concentrations of vacancies and oxygen ions, respectively.[62] Basically, the D_{vac} varies in an exponential manner with the Gibbs free energy of activation (ΔG_{mig}^{path}) for vacancy migration. By invoking the harmonic approximation to transition state theory, we have

$$D_{vac} = \frac{1}{6} d^2 \nu = \frac{1}{6} d^2 \frac{\prod_i^{3N} \nu_i^{initial}}{\prod_i^{3N-1} \nu_i^{saddle}} \exp\left(-\frac{\Delta G_{mig}^{path}}{RT} \right) \qquad (11)$$

where d is the distance over which the hop occurs, ν is the hopping frequency, and ν_i is the vibrational frequencies of normal nodes. As for the C_{vac}, if it is assumed to a first approximation that equilibrium is established during the formation of oxygen vacancies and gaseous O_2 from stoichiometric perovskites[86], then we have

$$K = \exp\left(-\frac{\Delta G_{f,vac}}{RT} \right) = \frac{C_{vac} P_{O_2}^{1/2}}{(1 - 2C_{vac})^2 (3 - C_{vac})} \qquad (12)$$

where K and $\Delta G_{f,vac}$ are the equilibrium constant and Gibbs free energy change for vacancy formation, respectively, and P_{O_2} is the partial pressure of O_2 in the gas phase. Given the fact that the experimentally measured vacancy concentration is on the order of 10^{-2} in the oxygen deficiency δ, it can be deduced from the equation that the C_{vac} is related to the $\Delta G_{f,vac}$ in an exponential fashion as well. Thus, the oxygen diffusion coefficient, which is roughly the product of the D_{vac} and C_{vac}, is expected to have an Arrhenius-like temperature dependence.

Since the $\Delta E_{f,vac}$ and ΔE_{mig}^{path} vary in much the same way, respectively, as the $\Delta G_{f,vac}$ and ΔG_{mig}^{path} do, plotting the logarithm of the oxygen diffusion coefficient against the sum of the $\Delta E_{f,vac}$ and ΔE_{mig}^{path} is expected to give a straight line. If we consider further that the $\Delta E_{f,vac}$ for each $LaMO_3$ takes a much higher value than the corre-

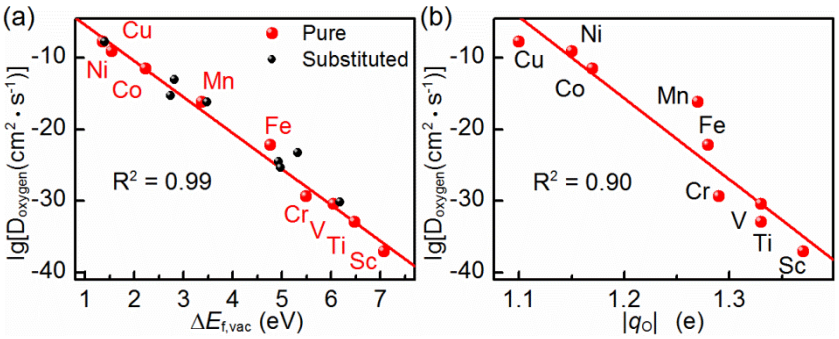

Figure 9. Dependence of the logarithm of D_{oxygen} on (a) $\Delta E_{f,vac}$ and on (b) $|q_O|$.

sponding ΔE_{mig}^{path} and hence dominates the sum, the oxygen transport kinetics should be determined predominantly by the oxygen vacancy formation energy and hence by the oxygen vacancy concentration. Here the oxygen diffusion coefficients are calculated at 900 °C and an O_2 partial pressure of 1 atm, the logarithm of which are then plotted as a function of the oxygen vacancy formation energy for all the La-based perovskites. Indeed, a very good linear scaling relation is established between these two quantities, as shown in Fig. 9a. In contrast, as the other component that is used to yield the diffusivity, the oxygen migration barrier is not capable of describing the variation in the diffusion coefficient (see Fig. S13). Moreover, in order to demonstrate that the relation between oxygen diffusion coefficient and oxygen vacancy formation energy can be extended to the substituted $LaMO_3$, the same calculations were performed in $LaFe_{0.5}M_{0.5}O_3$ (M = Sc - Mn and Co - Cu) as well. One can see in Fig. 9a that the diffusion coefficient and the vacancy formation energy are correlated in much the same way as that in the pure $LaMO_3$.

As mentioned earlier, the actual partial charge on either the oxygen or transition metal ion may explain the trend in the $\Delta E_{f,vac}$. It is therefore reasonable to expect that the oxygen transport kinetics in $LaMO_3$ is closely related to the degree to which the electron density is withdrawn by the oxygen ion in the stoichiometric structure. Fig. 9b depicts the variation of the logarithm of the oxygen diffusion coefficient as the partial charge on the oxygen ion is changed. The negative slope of the straight line means that the oxygen transport can be enhanced by lowering the electron density shift toward oxygen. This interesting and important effect has its origin in the relationship between the actual partial charge on either the oxygen or transition-metal ion and the strength of ionic bonding in $LaMO_3$.

4. Conclusion

In this work, plane wave DFT+U calculations have been carried out to understand the physical origin of the oxygen mobility difference in the $LaMO_3$ (M = Sc - Cu) perovskites. In general, the perovskites exhibit an increased reducibility as we move from $LaScO_3$ to $LaCuO_3$. The oxygen vacancy formation energy in $LaFeO_3$, however, is exceptionally high, regardless of the exchange-correlation functionals used and the crystal structures adopted, which can be explained by the significant lowering of the electron exchange stabilization upon oxygen removal. Through energy decomposition and electronic structure analysis, it is found that both the electrostatic potential energy of interaction between oxygen and the remaining oxide lattice and the energy released by the electron transfer upon formation of oxygen vacancy are intimately related to the number of the electrons gained by the remaining defective perovskite structure.

The GFO distortion plays a minor role in determining the activation energy for the oxygen migration elementary steps in perovskites, while the structural dimensionality has a major impact on the favorable oxygen diffusion pathway. In the pseudocubic and orthorhombic structures the *xy*-plane is preferred by the migrating oxygen, and in the rhombohedral structure the capability of reversible oxygen storage is strongly dependent on the kinetics of oxygen diffusion along the cell edge. There exists an abrupt decrease in the oxygen migration barrier on moving from $LaCrO_3$ to $LaMnO_3$, which can be attributed to the lowered degree of charge redistribution on the central transition-metal ion during the migration process. Linear scaling relations are established to show that the oxygen bulk diffusion coefficient is governed essentially by the oxygen concentration because the oxygen vacancy formation energy takes a much higher value than the oxygen migration barrier. The actual partial charge on the transition metal or oxygen ion explains the electronic origin of the different oxygen mobilities in $LaMO_3$, and the observed trend can be described by using the oxygen vacancy formation energy as a good descriptor, which may therefore guide the investigation toward perovskite materials with better oxygen transport properties.

ASSOCIATED CONTENT

Supporting Information.
The determination of the U_{eff} values, the cell parameters of the pseudocubic structures of $LaMO_3$, and the calculated results obtained by using the PBE+U method can be found in the Supporting Information.
This material is available free of charge via the Internet at http://pubs.acs.org.

AUTHOR INFORMATION

Corresponding Author

* Email: yanzhu@ecust.edu.cn

Notes

The authors declare no competing financial interest.

ACKNOWLEDGMENT

This work is supported by the Natural Science Foundation of China (21473053, 91645122, and U1663221), the National Key Research and Development Program of China (2018YFB0604700), and the Fundamental Research Funds for the Central Universities (222201718003). The computational time provided by the Notur project is highly acknowledged.

References

(1) Pena, M. A.; Fierro, J. L. G. Chemical Structures and Performance of Perovskite Oxides. *Chem. Rev.* **2001,** *101*, 1981-2017.

(2) Ormerod, R. M. Solid Oxide Fuel Cells. *Chem. Soc. Rev.* **2003,** *32*, 17-28.

(3) Royer, S.; Duprez, D.; Can, F.; Courtois, X.; Batiot-Dupeyrat, C.; Laassiri, S.; Alamdari, H. Perovskites as Substitutes of Noble Metals for Heterogeneous Catalysis: Dream or Reality. *Chem. Rev.* **2014,** *114*, 10292-10368.

(4) Wang, H.; Tablet, C.; Feldhoff, A.; Caro, J. A Cobalt-Free Oxygen-Permeable Membrane Based on the Perovskite-Type Oxide $Ba_{0.5}Sr_{0.5}Zn_{0.2}Fe_{0.8}O_{3-\delta}$. *Adv. Mater.* **2005,** *17*, 1785-1788.

(5) Ruiz-Morales, J. C.; Marrero-López, D.; Gálvez-Sánchez, M.; Canales-Vázquez, J.; Savaniu, C.; Savvin, S. N. Engineering of Materials for Solid Oxide Fuel Cells and Other Energy and Environmental Applications. *Energy Environ. Sci.* **2010,** *3*, 1670-1681.

(6) Munoz-Garcia, A. B.; Ritzmann, A. M.; Pavone, M.; Keith, J. A.; Carter, E. A. Oxygen Transport in Perovskite-Type Solid Oxide Fuel Cell Materials: Insights from Quantum Mechanics. *Acc. Chem. Res.* **2014,** *47*, 3340-3348.

(7) Orera, A.; Slater, P. R. New Chemical Systems for Solid Oxide Fuel Cells. *Chem. Mater.* **2009,** *22*, 675-690.

(8) Jacobson, A. J. Materials for Solid Oxide Fuel Cells. *Chem. Mater.* **2009,** *22*, 660-674.

(9) Wei, Y.; Yang, W.; Caro, J.; Wang, H. Dense Ceramic Oxygen Permeable Membranes and Catalytic Membrane Reactors. *Chem. Eng. J.* **2013,** *220*, 185-203.

(10) Kharton, V. V.; Yaremchenko, A. A.; Kovalevsky, A. V.; Viskup, A. P.; Naumovich, E. N.; Kerko, P. F. Perovskite-type Oxides for High-Temperature Oxygen Separation Membranes. *J. Membrane Sci.* **1999,** *163*, 307-317.

(11) Sunarso, J.; Baumann, S.; Serra, J. M.; Meulenberg, W. A.; Liu, S.; Lin, Y. S.; Diniz da Costa, J. C. Mixed Ionic–Electronic Conducting (MIEC) Ceramic-Based Membranes for Oxygen Separation. *J. Membrane Sci.* **2008,** *320*, 13-41.

(12) Mihai, O.; Chen, D.; Holmen, A. Chemical Looping Methane Partial Oxidation: the Effect of the Crystal Size and O Content of $LaFeO_3$. *J. Catal.* **2012,** *293*, 175-185.

(13) Pavone, M.; Muñoz-García, A. B.; Ritzmann, A. M.; Carter, E. A. First-Principles Study of Lanthanum Strontium Manganite: Insights into Electronic Structure and Oxygen Vacancy Formation. *J. Phys. Chem. C* **2014,** *118*, 13346-13356.

(14) Pavone, M.; Ritzmann, A. M.; Carter, E. A. Quantum-Mechanics-Based Design Principles for Solid Oxide Fuel Cell Cathode Materials. *Energy Environ. Sci.* **2011,** *4*, 4933-4937.

(15) Lee, Y. L.; Kleis, J.; Rossmeisl, J.; Shao-Horn, Y.; Morgan, D. Prediction of Solid Oxide Fuel Cell Cathode Activity with First-Principles Descriptors. *Energy Environ. Sci.* **2011,** *4*, 3966-3970.

(16) Chen, C.; Ciucci, F. Designing Fe-Based Oxygen Catalysts by Density Functional Theory Calculations. *Chem. Mater.* **2016,** *28*, 7058-7065.

(17) Kilner, J. A.; Brook, R. J. A Study of Oxygen Ion Conductivity in Doped Non-Stoichiometric Oxides. *Solid State Ionics* **1982,** *6*, 237-252.

(18) Sammells, A. F.; Cook, R. L.; White, J. H.; Osborne, J. J.; MacDuff, R. C. Rational Selection of Advanced Solid Electrolytes for Intermediate Temperature Fuel Cells. *Solid State Ionics* **1992,** *52*, 111-123.

(19) Mogensen, M.; Lybye, D.; Bonanos, N.; Hendriksen, P. V.; Poulsen, F. W. Factors Controlling the Oxide Ion Conductivity of Fluorite and Perovskite Structured Oxides. *Solid State Ionics* **2004,** *174*, 279-286.

(20) Wessel, C.; Lumey, M. W.; Dronskowski, R. First-Principles Electronic-Structure Calculations on the Stability and Oxygen Conductivity in $Ba_{0.5}Sr_{0.5}Co_{0.8}Fe_{0.2}O_{3-\delta}$. *J. Membrane Sci.* **2011,** *366*, 92-96.

(21) Gilleßen, M.; Lumeij, M.; George, J.; Stoffel, R.; Motohashi, T.; Kikkawa, S.; Dronskowski, R. Oxygen-Storage Materials $BaYMn_2O_{5+\delta}$ from the Quantum-Chemical Point of View. *Chem. Mater.* **2012,** *24*, 1910-1916.

(22) Mayeshiba, T. T.; Morgan, D. D. Factors Controlling Oxygen Migration Barriers in Perovskites. *Solid State Ionics* **2016,** *296*, 71-77.

(23) Mastrikov, Y. A.; Merkle, R.; Kotomin, E. A.; Kuklja, M. M.; Maier, J. Formation and Migration of Oxygen Vacancies in $La_{1-x}Sr_xCo_{1-y}Fe_yO_{3-\delta}$ Perovskites: Insight from Ab Initio Calculations and Comparison with $Ba_{1-x}Sr_xCo_{1-y}Fe_yO_{3-\delta}$. *Phys. Chem. Chem. Phys.* **2013,** *15*, 911-918.

(24) Ritzmann, A. M.; Muñoz-García, A. B.; Pavone, M.; Keith, J. A.; Carter, E. A. Ab Initio DFT+U Analysis of Oxygen Vacancy Formation and Migration in $La_{1-x}Sr_xFeO_{3-\delta}$ (x = 0, 0.25, 0.50). *Chem. Mater.* **2013,** *25*, 3011-3019.

(25) Kresse, G.; Hafner, J. Ab Initio Molecular Dynamics for Open-Shell Transition Metals. *Phys. Rev. B* **1993,** *48*, 13115-13118.

(26) Kresse G, F. J. Efficiency of Ab-Initio Total Energy Calculations for Metals and Semiconductors Using A Plane-Wave Basis Set. *Comp. Mater. Sci.* **1996,** *6*, 15-50.

(27) Kresse, G.; Furthmüller, J. Efficient Iterative Schemes for Ab Initio Total-Energy Calculations Using a Plane-Wave Basis Set. *Phys. Rev. B* **1996,** *54*, 11169-11186.

(28) Kresse, G. From Ultrasoft Pseudopotentials to the Projector Augmented-Wave method. *Phys. Rev. B* **1999,** *59*, 1758-1775.

(29) Wellendorff, J.; Lundgaard, K. T.; Møgelhøj, A.; Petzold, V.; Landis, D. D.; Nørskov, J. K.; Bligaard, T.; Jacobsen, K. W. Density Functionals for Surface Science: Exchange-Correlation Model Development with Bayesian Error Estimation. *Phys. Rev. B* **2012,** *85*, 5826-5831.

(30) Perdew, J. P.; Burke, K.; Ernzerhof, M. Generalized Gradient Approximation Made Simple. *Phys. Rev. Lett.* **1996,** *77*, 3865-3868.

(31) Cesare, F. Hybrid Functionals Applied to Perovskites. *J. Phys.: Condens. Matter* **2014,** *26*, 253202.

(32) Perdew, J. P.; Wang, Y. Accurate and Simple Analytic Representation of the Electron-Gas Correlation Energy. *Phys. Rev. B* **1992,** *45*, 13244-13249.

(33) Lee, K.; Murray, É. D.; Kong, L.; Lundqvist, B. I.; Langreth, D. C. A Higher-Accuracy van der Waals Density Functional. *Phys. Rev. B* **2010,** *82*, 081101.

(34) Cohen, A. J.; Mori-Sanchez, P.; Yang, W. T. Insights Into Current Limitations of Density Functional Theory. *Science* **2008,** *321*, 792-794.

(35) Anisimov VI, V. I.; Zaanen, J.; Andersen, O. K. Band Theory and Mott Insulators: Hubbard U Instead of Stoner I. *Phys. Rev. B: Condens. Matter* **1991,** *44*, 943-954.

(36) Anisimov V. I. , Z. J., and Andersen O. K. First-Principles Calculations of the Electronic Structure and Spectra of Strongly Correlated Systems: the LDA+U Method. *J. Phys.: Condens. Matter* **1997,** *9*, 767-807.

(37) Dudarev, S.; Botton, G.; Savrasov, S.; Humphreys, C.; Sutton, A. Electron-Energy-Loss Spectra and the Structural

Stability of Nickel Oxide: An LSDA+U Study. *Phys. Rev. B* **1998,** *57*, 1505-1509.
(38) Wang, L.; Maxisch, T.; Ceder, G. Oxidation Energies of Transition Metal Oxides Within the GGA+U Framework. *Phys. Rev. B* **2006,** *73*, 195107.
(39) Jain, A.; Hautier, G.; Ong, S. P.; Moore, C. J.; Fischer, C. C.; Persson, K. A.; Ceder, G. Formation Enthalpies by Mixing GGA and GGA+U Calculations. *Phys. Rev. B* **2011,** *84*, 045115.
(40) Ritzmann, A. M.; Pavone, M.; Muñoz-García, A. B.; Keith, J. A.; Carter, E. A. Ab Initio DFT+U Analysis of Oxygen Transport in $LaCoO_3$: The Effect of Co^{3+} Magnetic States. *J. Mater. Chem. A* **2014,** *2*, 8060-8074.
(41) Monkhorst, H. J. Special Points for Brillouin-Zone Integrations. *Phys. Rev. B: Condens. Matter* **1976,** *13*, 5188-5192.
(42) Abbate, M.; Fuggle, J. C.; Fujimori, A.; Tjeng, L. H.; Chen, C. T.; Potze, R.; Sawatzky, G. A.; Eisaki, H.; Uchida, S. Electronic Structure and Spin-State Transition of $LaCoO_3$. *Phys. Rev. B* **1993,** *47*, 16124-16130.
(43) Maris, G.; Ren, Y.; Volotchaev, V.; Zobel, C.; Lorenz, T.; Palstra, T. T. M. Evidence for Orbital Ordering in $LaCoO_3$. *Phys. Rev. B* **2003,** *67*, 224423.
(44) Haverkort, M. W.; Hu, Z.; Cezar, J. C.; Burnus, T.; Hartmann, H.; Reuther, M.; Zobel, C.; Lorenz, T.; Tanaka, A.; Brookes, N. B.; et al. Spin State Transition in $LaCoO_3$ Studied Using Soft X-ray Absorption Spectroscopy and Magnetic Circular Dichroism. *Phys. Rev. Lett.* **2006,** *97*, 176405.
(45) Henkelman, G.; Jónsson, H. Improved Tangent Estimate in the Nudged Elastic Band Method for Finding Minimum Energy Paths and Saddle Points. *J. Chem. Phys.* **2000,** *113*, 9978-9985.
(46) Henkelman, G.; Uberuaga, B. P.; Jónsson, H. A Climbing Image Nudged Elastic Band Method for Finding Saddle Points and Minimum Energy Paths. *J. Chem. Phys.* **2000,** *113*, 9901-9904.
(47) Sheppard, D.; Terrell, R.; Henkelman, G. Optimization Methods for Finding Minimum Energy Paths. *J. Chem. Phys.* **2008,** *128*, 134106.
(48) Zhu, Y.; Chen, D.; Zhou, X.; Yuan, W. DFT Studies of Dry Reforming of Methane on Ni Catalyst. *Catal. Today* **2009,** *148*, 260-267.
(49) Glazer, A. M. The Classification of Tilted Octahedra in Perovskites. *Acta. Crystallogr.* **1972,** *28*, 3384-3392.
(50) Lufaso, M. W.; Woodward, P. M. Prediction of the Crystal Structures of Perovskites Using the Software Program SPuDS. *Acta. Crystallogr., Sect. B: Struct. Sci.* **2001,** *57*, 725-738.
(51) Jahn, H. A.; Teller, E. Stability of Polyatomic Molecules in Degenerate Electronic States I-Orbital Degeneracy. *Proc. R. Soc. Lond. A* **1937,** *161*, 220-235.
(52) Jahn, H. Stability of Polyatomic Molecules in Degenerate Electronic States II-Spin Degeneracy. *Proc. R. Soc. Lond. A* **1938,** *164*, 117-131.
(53) Woodward, P. M. Octahedral Tilting in Perovskites. I. Geometrical Considerations. *Acta. Crystallogr., Sect. B: Struct. Sci.* **1997,** *53*, 32-43.
(54) Woodward, P. M. Octahedral Tilting in Perovskites. II. Structure Stabilizing Forces. *Acta. Crystallogr., Sect. B: Struct. Sci.* **1997,** *53*, 44–66.
(55) Wilson, J. A. The Energy-Resolved STM results, Their Apparent Inhomogeneity and the True Bulk Behaviour of the HTSC Cuprates, from a Negative-U Perspective. *J. Phys-Condens. Mat.* **2007,** *19*, 106224.
(56) Zhou, J. S.; Goodenough, J. B. Paramagnetic Phase in Single-Crystal $LaMnO_3$. *Phys. Rev. B* **1999,** *60*, 15002-15004.
(57) Zobel, C.; Kriener, M.; Bruns, D.; Baier, J.; Grüninger, M.; Lorenz, T.; Reutler, P.; Revcolevschi, A. Evidence for a Low-Spin to Intermediate-Spin State Transition in $LaCoO_3$. *Phys. Rev. B* **2002,** *66*, 020402.
(58) Sanchez, M. C.; Subias, G.; Garcia, J.; Blasco, J. Cooperative Jahn-Teller Phase Transition in $LaMnO_3$ Studied by X-Ray Absorption Spectroscopy. *Phys. Rev. Lett.* **2003,** *90*, 045503.
(59) Kováčik, R.; Ederer, C. Calculation of Model Hamiltonian Parameters for $LaMnO_3$ Using Maximally Localized Wannier Functions. *Phys. Rev. B* **2010,** *81*, 245108.
(60) Murnaghan, F. D. The Compressibility of Media Under Extreme Pressures. *P. Natl. Acad. Sci.* **1944,** *30*, 244-247.
(61) Mars, P.; van Krevelen, D. W. Oxidations Carried Out By Means of Vanadium Oxide Catalysts. *Chem. Eng. Sci.* **1954,** *3*, 41-59.
(62) Ishigaki, T.; Yamauchi, S.; Kishio, K.; Mizusaki, J.; Fueki, K. Diffusion of Oxide Ion Vacancies in Perovskite-Type Oxides. *J. Solid State Chem.* **1988,** *73*, 179-187.
(63) Islam, M. S. Computer Modelling of Defects and Transport in Perovskite Oxides. *Solid State Ionics* **2002,** *154-155*, 75-85.
(64) Kilner, J.; Berenov, A.; Rossiny, J., Diffusivity of the Oxide Ion in Perovskite Oxides. In *Perovskite Oxide for Solid Oxide Fuel Cells*, Ishihara, T., Ed. Springer: 2009; pp 95-116.
(65) Jones, A.; Islam, M. S. Atomic-Scale Insight into $LaFeO_3$ Perovskite: Defect Nanoclusters and Ion Migration. *J. Phys. Chem. C* **2008,** *112*, 4455-4462.
(66) Yang, Q.; Cao, J. X.; Ma, Y.; Zhou, Y. C.; Jiang, L. M.; Zhong, X. L. Strain Effects on Formation and Migration Energies of Oxygen Vacancy in Perovskite Ferroelectrics: A First-Principles Study. *J. Appl. Phys.* **2013,** *113*, 184110.
(67) Curnan, M. T.; Kitchin, J. R. Effects of Concentration, Crystal Structure, Magnetism, and Electronic Structure Method on First-Principles Oxygen Vacancy Formation Energy Trends in Perovskites. *J. Phys. Chem. C* **2014,** *118*, 28776-28790.
(68) Nowotny, J.; Rekas, M. Defect Chemistry of (La, Sr) MnO_3. *J. Am. Ceram. Soc.* **1998,** *81*, 67-80.
(69) Mizusaki, J.; Yoshihiro, M.; Yamauchi, S.; Fueki, K. Nonstoichiometry and Defect Structure of the Perovskite-Type Oxides $La_{1-x}Sr_xFeO_{3-\delta}$. *J. Solid State Chem.* **1985,** *58*, 257-266.
(70) Mizusaki, J.; Mima, Y.; Yamauchi, S.; Fueki, K.; Tagawa, H. Nonstoichiometry of the Perovskite-Type Oxides $La_{1-x}Sr_xCoO_{3-\delta}$. *J. Solid State Chem.* **1989,** *80*, 102-111.
(71) Nomura, K.; Kageyama, H.; Ohmi, K.; Fujita, M.; Ueda, T. Chemical Reactivities of $LaScO_3$-Based Perovskite Oxides and Platinum. *Chem. Lett.* **2013,** *42*, 1268-1270.
(72) Grieken R. van, P. J. L., Lucas A.,Calleja G., Rojas M. L., Fierro J. L.G. Selective Production of Methanol from Syngas over $LaTi_{1-x}Cu_xO_3$ Mixed Oxide. *Catal. Lett.* **1991,** *8*, 335-344.
(73) Tascón, J. M. D.; Tejuca, L. G. Catalytic Activity of Perovskite-Type Oxides $LaMeO_3$. *React. Kinet. Catal. Lett.* **1980,** *15*, 185-191.
(74) Santana, J. A.; Krogel, J. T.; Kent, P. R. C.; Reboredo, F. A. Diffusion Quantum Monte Carlo Calculations of $SrFeO_3$ and $LaFeO_3$. *J Chem. Phys.* **2017,** *147*, 034701.
(75) Lee, Y. L.; Kleis, J.; Rossmeisl, J.; Morgan, D. Ab Initio Energetics of $LaBO_3$(001) (B=Mn, Fe, Co, and Ni) for Solid Oxide Fuel Cell Cathodes. *Phys. Rev. B* **2009,** *80*, 224101.
(76) Goodenough, J. B. *Magnetism and the Chemical Bond, Interscience Monographs on Chemistry*. Nabu Press: N.Y, 1963; Vol. 1, pp 157-184.
(77) Izgorodina, E. I.; Bernard, U. L.; Dean, P. M.; Pringle, J. M.; MacFarlane, D. R. The Madelung Constant of Organic Salts. *Cryst. Growth Des.* **2009,** *9*, 4834-4839.
(78) Zhang, L.; Liu, B.; Zhuang, H.; Kent, P. R. C.; Cooper, V. R.; Ganesh, P.; Xu, H. Oxygen Vacancy Diffusion in Bulk $SrTiO_3$ from Density Functional Theory Calculations. *Comp. Mat. Sci.* **2016,** *118*, 309-315.
(79) Mayeshiba, T.; Morgan, D. Strain Effects on Oxygen Migration in Perovskites. *Phys. Chem. Chem. Phys.* **2015,** *17*, 2715-2721.

(80) Tealdi, C.; Mustarelli, P. Improving Oxygen Transport in Perovskite-Type $LaGaO_3$ Solid Electrolyte through Strain. *J. Phys. Chem. C* **2014,** *118*, 29574-29582.
(81) Bassat, J.; Burriel, M.; Wahyudi, O.; Castaing, R.; Ceretti, M.; Veber, P.; Weill, I.; Villesuzanne, A.; Grenier, J.; Paulus, W.; et al. Anisotropic Oxygen Diffusion Properties in $Pr_2NiO_{4+\delta}$ and $Nd_2NiO_{4+\delta}$ Single Crystals. *J. Phys. Chem. C* **2013,** *117*, 26466–26472.
(82) Burriel, M.; Garcia, G.; Santiso, J.; Kilner, J. A.; Chater, R. J.; Skinner, S. J. Anisotropic Oxygen Diffusion Properties in Epitaxial Thin Films of $La_2NiO_{4+\delta}$. *J. Mater. Chem.* **2008,** *18*, 416-422.
(83) Belzner, A.; Gür, T. M.; Huggins, R. A. Oxygen Chemical Diffusion in Strontium Doped Lanthanum Manganites. *Solid State Ionics* **1992,** 57, 327-337.
(84) Islam, M. S. Ionic Transport in ABO_3 Perovskite Oxides a Computer Modelling Tour. *J. Mater. Chem.* **2000,** *10*, 1027-1038.
(85) Cherry, M.; Islam, M. S.; Catlow, C. R. A. Oxygen Ion Migration in Perovskite-Type Oxides. *J. Solid State Chem.* **1995,** *118*, 125-132.
(86) Holt, A.; Norby, T.; Glenne, R. Defects and Transport in $SrFe_{1-x}Co_xO_{3-\delta}$. *Ionics* **1999,** 5, 434-443.

TOC Graphic